RSC Advances

PAPER

View Article Online
View Journal | View Issue

Check for updates

Cite this: RSC Adv., 2021, 11, 19283

Received 11th March 2021
Accepted 26th April 2021

DOI: 10.1039/d1ra01941d

rsc.li/rsc-advances

Interface enriched highly interlaced layered MoS_2/NiS_2 nanocomposites for the photocatalytic degradation of rhodamine B dye†

S. Harish, *[a] P. Bharathi,[a] Prachi Prasad,[a] R. Ramesh, [c] S. Ponnusamy,[a] M. Shimomura, [d] J. Archana [a] and M. Navaneethan *[ab]

In the past few decades, air and water pollution by organic dyes has become a serious concern due to their high toxicity. Removal of these organic dyes from polluted water bodies is a serious environmental concern and the development of new advanced photocatalytic materials for decomposing organic dyes can be a good solution. In this work, layered molybdenum disulfide/nickel disulfide (MoS_2/NiS_2) nanocomposites with various NiS_2 content was synthesized by a one-step hydrothermal method using citric acid as a reducing agent. The X-ray diffraction pattern shows the hexagonal and cubical crystal structure of MoS_2 and NiS_2, respectively. Morphological analysis confirms the formation of MoS_2/NiS_2 nanosheets. The elemental composition of the samples was carried out by XPS, which shows a significant interaction between NiS_2 and MoS_2. The photocatalytic performance of MoS_2/NiS_2 nanocomposites was studied by the degradation of rhodamine B (RhB). Ni-4 sample shows higher photocatalytic activity with a maximum degradation of 90.61% under visible light irradiation for 32 min.

1. Introduction

Almost 15% of the net dye production is released in textile effluents into water bodies resulting in an unbalanced aquatic ecosystem and water pollution.[1] Photocatalysis is one of the dye degradation method which has attained more attention due to its large-scale applicability. Various semiconducting metal sulfides such as MoS_2, ZnS, CdS and CuS have been examined to degrade the pollutants using solar energy.[2–6] It mainly depends on several factors such as photon absorption ability, separation of ions, and transport rate of the photogenerated electrons and holes in the presence of light energy. Unique properties of MoS_2 such as tunable bandgap, reliability, low cost, thermal stability, excellent electronic[7,8] and optical properties which severs as potential material for photocatalysis, biosensors, memory, capacitors and other electronic devices.[9,10]

The 2-D layered structure of MoS_2 explored more due to its higher adsorption ability towards the degradation of organic compounds. The versatility of MoS_2 is endorsed by its unique layered structure with weakly coupled S–Mo–S sheets that makes the material extremely potential candidate. The bond within the layers are highly covalent, whereas the interaction between the adjacent layers are remarkably weak van der Waal's interaction.[11] This contributes to facile basic cleavage and marked anisotropy property to the crystal structure. Essentially, the layered MoS_2 structure possesses a large surface area and massive active sites and tunable bandgap, which can provide sufficient contact for effective photocatalytic reactions. However, the photocatalytic property of MoS_2 was limited due to the rapid recombination of photoinduced electrons (e^-) and holes (h^+).[12] The close contact between MoS_2 and NiS_2 will remarkedly improve the conductivity and provide synergistic effect, further leading to increase in catalytic activity. The unique structure of these materials can provide more active sites and higher contact areas with organic pollutants. The formation of heterostructure distinctly decrease the recombination rate which enhances the photocatalytic performance.[13,14]

Many researchers have synthesized various composites with MoS_2 to increase the degradation efficiency and to reduce the recombination rate. Yong Ding *et al.* synthesized MoS_2/rGO composite hydrogel by hydrothermal method and obtained 99% of degradation of methylene blue in 60 min.[15] Hui Feng *et al.* have synthesized ZnS/CdS–Mn/MoS_2/TiO_2 by simple hydrothermal method followed by SILAR. It showed good stability towards MO dye under solar light irradiation with the removal rate of 98% in 100 min.[16] Wei Yang Lim *et al.* has studied the interaction of $ZnIn_2S_4$/transition metal chalcogenides for dye degradation. Among them, the $ZnIn_2S_4$/MoS_2

---

[a] Functional Materials and Energy Devices Laboratory, Department of Physics and Nanotechnology, SRM Institute of Science and Technology, Kattankulathur, 603 203, India. E-mail: aravindharri@gmail.com; m.navaneethan@gmail.com

[b] Nanotechnology Research Center (NRC), Faculty of Engineering and Technology, SRM Institute of Science and Technology, Chennai, 603203, Tamil Nadu, India

[c] Department of Physics, Periyar University, Salem 636011, India

[d] Graduate School of Science and Technology, Shizuoka University, 3-5-1 Johoku, Naka-Ku, Hamamatsu, Shizuoka 432-8011, Japan

† Electronic supplementary information (ESI) available. See DOI: 10.1039/d1ra01941d

composite exhibits superior MO degradation under visible light irradiation.[17] Xin Li *et al.* demonstrated a MoS_2/SnS heterostructure for promising photocatalytic performance using first principle investigation. This composite has formed type-II heterostructure which facilitates the spatial separation and migration of photoexcited electron–hole pairs under solar light irradiation.[18]

Xuan Chen *et al.* have synthesized MnS/MoS_2 nanolayered heterojunction for the degradation of RhB dye. Compared to pristine MnS, MnS/MoS_2 composites showed 161% enhancement in photocatalytic performance.[19] Xing-Liang Yin *et al.* have prepared $CdS@MoS_2$ core@shell heterostructure by facile solvothermal method. The retarding charge recombination and photo corrosion of $CdS@MoS_2$ leads to high efficiency and stability over RhB photocatalytic dye degradation.[20] Yaqing Yang *et al.* proposed the fabrication process of $MoS_2–Ni_3S_2$ hetero-nanorods supported by Ni foam $MoS_2–Ni_3S_2$ HNRs/NF *via* hydrothermal method. The well-exposed active sites of Ni_3S_2 and MoS_2 and their heterointerfaces paved the enhanced activity of HER, OER, and overall water splitting.[21] In another work, Molla *et.al*. has synthesized nickel sulfide nanoparticles with tunable bandgap and examined the degradation of various organic dyes (crystal violet (CV), rhodamine B (RhB), methylene blue (MB), Nile blue (NB), and black T (EBT)) in the presence and the absence of light.[22–24]

In addition to that the MoS_2/NiS_2 structure may involve highly dispersed MoS_2 nanosheets. Considering this, such dispersed nanosheets can be efficiently used to control the recombination rate in MoS_2 as it is forming numerous nano interfaces with NiS_2. Till date, there are no studies on photocatalytic dye degradation based on MoS_2/NiS_2 nanocomposites. In this work, the facile synthesis of MoS_2/NiS_2 nanocomposites was carried out by the hydrothermal method with different concentrations of Ni precursors. The photocatalytic activity of the samples is evaluated by the degradation rate of rhodamine B under visible light irradiation.

2. Experimental section

All the chemical reagents were of analytical grade and used without any further purification. Sodium molybdate dehydrate ($Na_2MoO_42H_2O$), nickel acetate ($Ni(CH_3CO_2)_2 \cdot 4H_2O$), thioacetamide ($C_2H_5NS$), and citric acid ($C_6H_8O_7$), were purchased from Wako Chemicals, Japan.

2.1. Synthesis of MoS_2/NiS_2 nanocomposites

In a typical reaction, 0.04 M of sodium molybdate dihydrate and 0.08 M of thioacetamide was dissolved in 50 mL of DI-water. Then 0.04 M citric acid was added into the above solution and it allowed to stir overnight with the addition of different concentration of nickel acetate. Finally, the mixture was transferred into a Teflon-lined autoclave and maintained at 180 °C for 24 h. The obtained precipitate was separated by centrifugation and washed several times with DI-water and ethanol. The obtained product was dried at 80 °C for 10 h. The sample denoted as Ni-1 (0.005 M), Ni-2 (0.010 M), Ni-3 (0.015 M) and Ni-4 (0.02 M) respectively. The same procedure was followed to synthesis MoS_2 without nickel addition and denoted as MoS_2.

2.2. Characterization of MoS_2/NiS_2 nanosheets

The structure of the product was characterized by a Rigaku X-ray diffractometer (XRD) (RINT 2200, Japan) with CuKα ($\lambda = 1.5418$ Å) radiation with a step interval of 0.02° s^{-1}. The morphological analysis was carried out by a field emission scanning electron microscope (FESEM) (JEOL JSM 7001F microscope) at an accelerating voltage of 15 kV and a transmission electron microscope (TEM) (JEOL JEM 2100F microscope) at an accelerating voltage of 200 kV. UV-vis spectroscopy analyses were performed by a Shimadzu 3100 PC spectrophotometer (Japan). X-ray photoelectron spectroscopy (XPS) was performed by a Shimadzu ESCA 3400 (Japan).

2.3. Photocatalytic properties

The photocatalytic properties of synthesized samples were examined by the photo-assisted degradation method using rhodamine blue (RhB) as a model dye, at room temperature under a xenon light source (MAX-303, Asahi Spectra) as a source of visible-light irradiation. Before light irradiation, the RhB solution was prepared by adding 2 mg dye in 100 mL DI water, then a known amount of photocatalyst was added and the mixture was stirred under the dark condition to stabilize and equilibrate the adsorption of RhB onto the surface of the catalyst. The reaction mixture was then allowed to stir under the visible lamp which was positioned at 15 cm above the reaction mixture. At regular time intervals, 6 mL of the suspension was collected, centrifuged, and analyzed by a UV-vis spectrometer (Shimadzu 3100 PC spectrophotometer, Japan). The degradation of RhB was quantified from the decrease in the intensity of

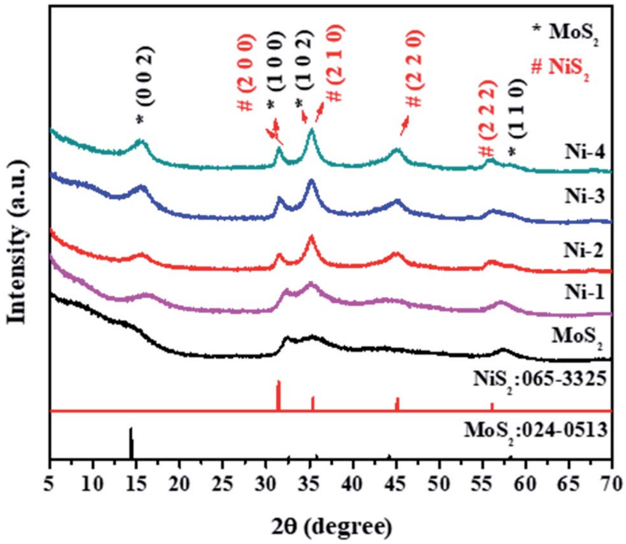

Fig. 1 XRD patterns of MoS_2/NiS_2 nanocomposites with varied NiS_2 contents.

the associated characteristic absorption. The photodegradation percentage of RhB was calculated using the following equation:

$$D(\%) = \frac{(C_t - C_0)}{C_0} \times 100$$

where C_0 and C_t are the concentrations of RhB at time 0 and t (s), respectively, and t is the irradiation time. The catalyst was regained by centrifugation and re-dispersed in the RhB solution for the recycling tests.

3. Results and discussion

3.1. Structural properties

The structural analysis of the samples was performed by powder XRD. Fig. 1 shows the XRD pattern of MoS_2 and MoS_2/NiS_2 nanocomposites. The characteristic peaks of the pure crystalline hexagonal phase of MoS_2 (molybdenite, JCPDS card no.024-0513) with lattice constants of $a = b = 3.16$ Å, $c = 12.29$ Å, respectively are observed at $2\theta = 14.2°, 32.5°, 35.2°, 44.3°, 57.4°,$

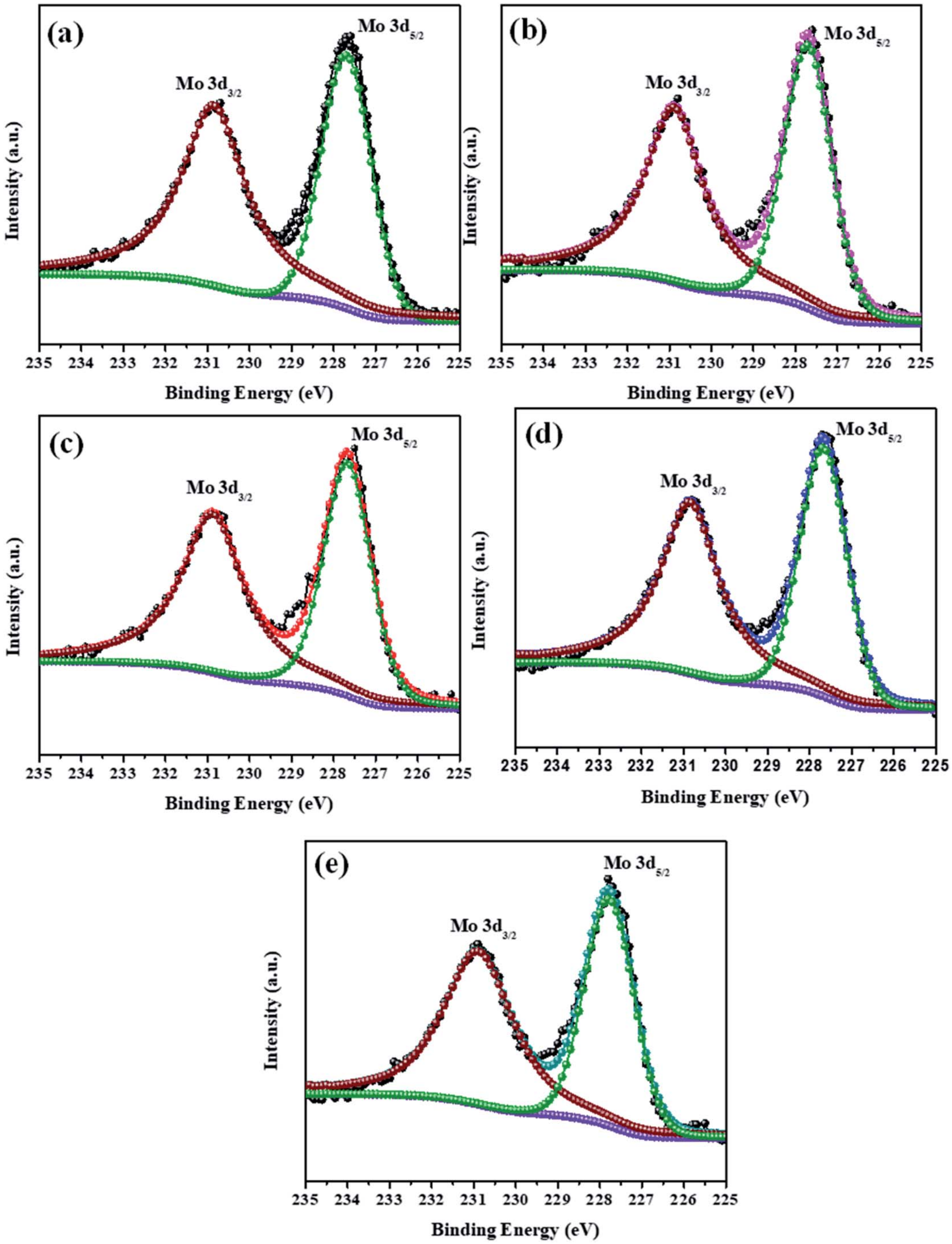

Fig. 2 XPS spectra of Mo 3d peak of MoS_2/NiS_2 nanocomposites with varied NiS_2 contents.

which can be assigned to (002), (100), (102) and (110) planes.[2] As the concentration of Ni was increased, the plane intensity of pure MoS_2 (002), (100), (102) and (110) peaks were also increased. The plane (100) of MoS_2 gets slightly shifted to a lower value and appears to merge with the NiS_2 (200) peak. It indicates that S has the same contribution to both MoS_2 and NiS_2. The NiS_2 diffraction plane (200), (210), (220), and (222) were observed which corresponds to the cubic structure of NiS_2 (JCPDS 065-3325).[25] No other impurities have appeared.

3.2. Optical properties

The UV-vis spectra of all the prepared samples have been shown in Fig. S1.† The spectra showed a strong excitation peak at the visible region and after the introduction of NiS_2, samples significantly extended towards the higher wavelength as compared to the pure sample. The absorbance peak value of pristine MoS_2 was observed at 760 nm.[26] The electrons were easily transformed from MoS_2 to NiS_2 due to the formation of heterostructure.[27]

3.3. Chemical compositional properties

The elemental composition analysis of the samples was carried out by XPS. The high-resolution XPS spectra of the Mo 3d and S 2p peaks of all samples (MoS_2–Ni-4) are demonstrated in the Fig. 2 and 3. The core level spectra of Mo 3d peaks confirm, two asymmetric peaks centred at 230.9 eV and 227.6 eV corresponding to the Mo $3d_{3/2}$ and $3d_{5/2}$ state with spin–orbit splitting energy difference of 3.3 eV.[28] After the formation of MoS_2/NiS_2 composite, the peak position of Mo 3d has slightly shifted towards higher value from 227.6 eV to 227.7 eV and 230.9 eV to 231.0 eV. These small shift attributed to the interaction of NiS_2 and MoS_2. Fig. 3 shows S 2p core-level spectra, in which the deconvoluted two asymmetric peaks at 161.1 eV and 162.4 eV are present, which corresponds to $2p_{3/2}$ and $2p_{1/2}$ and it indicates the formation of divalent sulfide ions (S^{2-}), with the separation energy of 1.3 eV. After the incorporation of NiS_2, the peaks $2p_{3/2}$ and $2p_{1/2}$ shifted to higher binding energy from 161.1 eV to 161.2 eV and 162.4 eV to 162.6 eV respectively with a peak splitting of 1.4 eV. This implied the existence of strong electronic interaction between Mo–S and Ni–S in MoS_2/NiS_2 nanocomposites. The S $2p_{3/2}$ peak was attributed to the typical metal–S bond, and S $2p_{1/2}$ corresponds to the sulfur defects.[29] Among all other samples, the intensity of S $2p_{1/2}$ (Ni-4) was slightly increased due to the sulfur vacancy after the incorporation of 0.02 M Ni. This plays a vital role in the photocatalytic reactivity which enhances the degradation percentage.[30]

The survey spectra of all the prepared samples are shown in Fig. S2(a).† It confirms the contribution of the elements without any impurities. The high-resolution spectra of the Ni 2p are showed in the Fig. S2(b).† The two asymmetric peaks are centred at 853.5 eV and 870.5 eV which corresponds to Ni $2p_{3/2}$ and Ni $2p_{1/2}$, respectively. This specifies the presence of Ni^{4+} state with the separation energy of 17 eV.[31] As the concentration of NiS_2 increases, the peak intensity of Ni 2p states also increase from Ni-1 to Ni-4 sample. Thus, XPS spectra provided evidence of the significant formation of NiS_2 and MoS_2 nanocomposites.

3.4. Morphological properties

The surface morphology of the prepared samples was characterized by FESEM, as shown in Fig. 4(a–e1). The morphology of

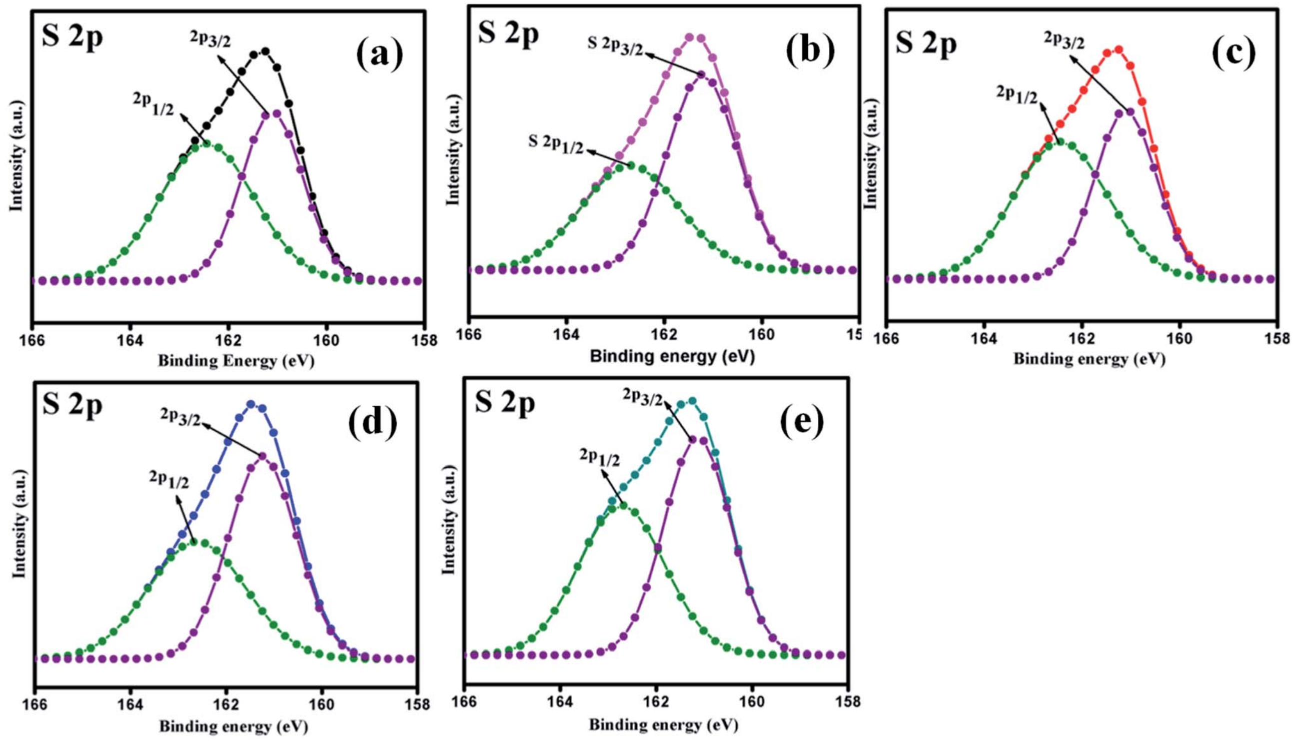

Fig. 3 XPS spectra of S 2p peak of MoS_2/NiS_2 nanocomposites with varied NiS_2 contents.

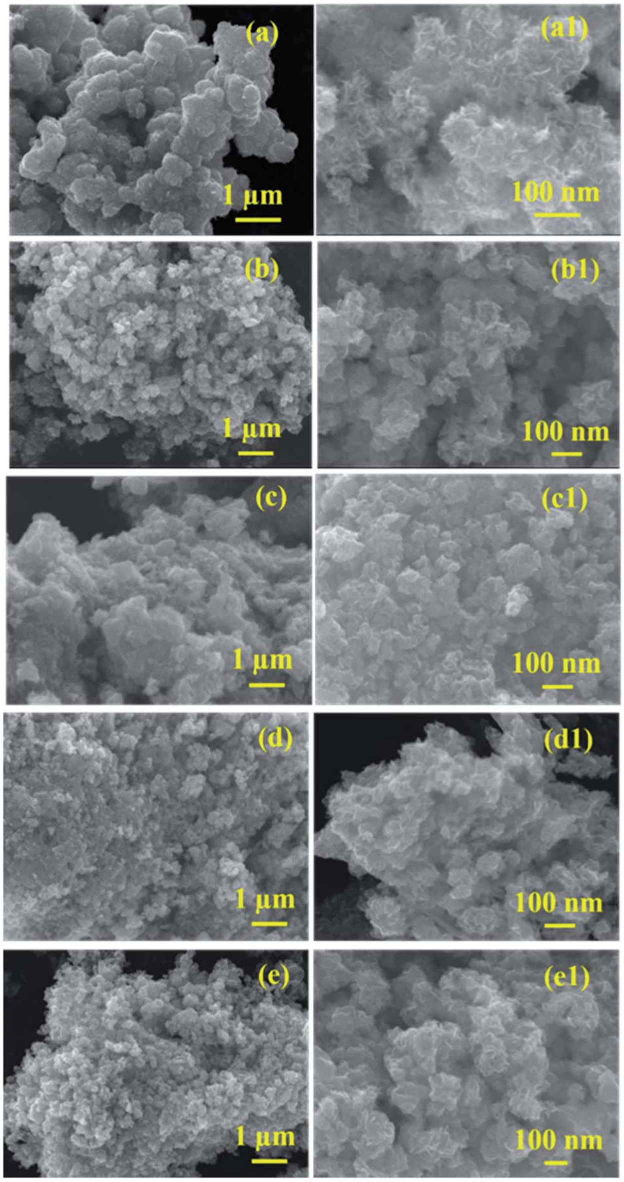

Fig. 4 (a–a1) FESEM images of MoS_2, (b–e1) FESEM images of MoS_2/NiS_2 nanocomposites with varied NiS_2 contents.

the pristine MoS_2 (Fig. 4(a and a1)) indicates the formation of spherical particles composed of nanosheets. Fig. 4(b–e1) reveals the morphology of MoS_2/NiS_2 composites (Ni-1–Ni-4). The spherical shape-like sheets are tends to agglomerate with an increase in the concentration of NiS_2. The HRTEM images of the prepared samples are shown in Fig. 5(a–e1). The crystallinity nature of pure MoS_2 has been increased with addition of NiS_2. Fig. 5a1 shows interplanar distance of 6.4 Å which corresponds to the plane (0 0 2) of MoS_2. The interlayer distance for NiS_2 shows around 2.8 Å which is corresponds to the plane (2 0 0) (Fig. 5b1). Fig. S3† implies the EDS mapping of MoS_2/NiS_2 nanocomposite of sample Ni-4. It confirms the uniform distribution of molybdenum, sulfur and nickel in the nanocomposite matrix.[30,32]

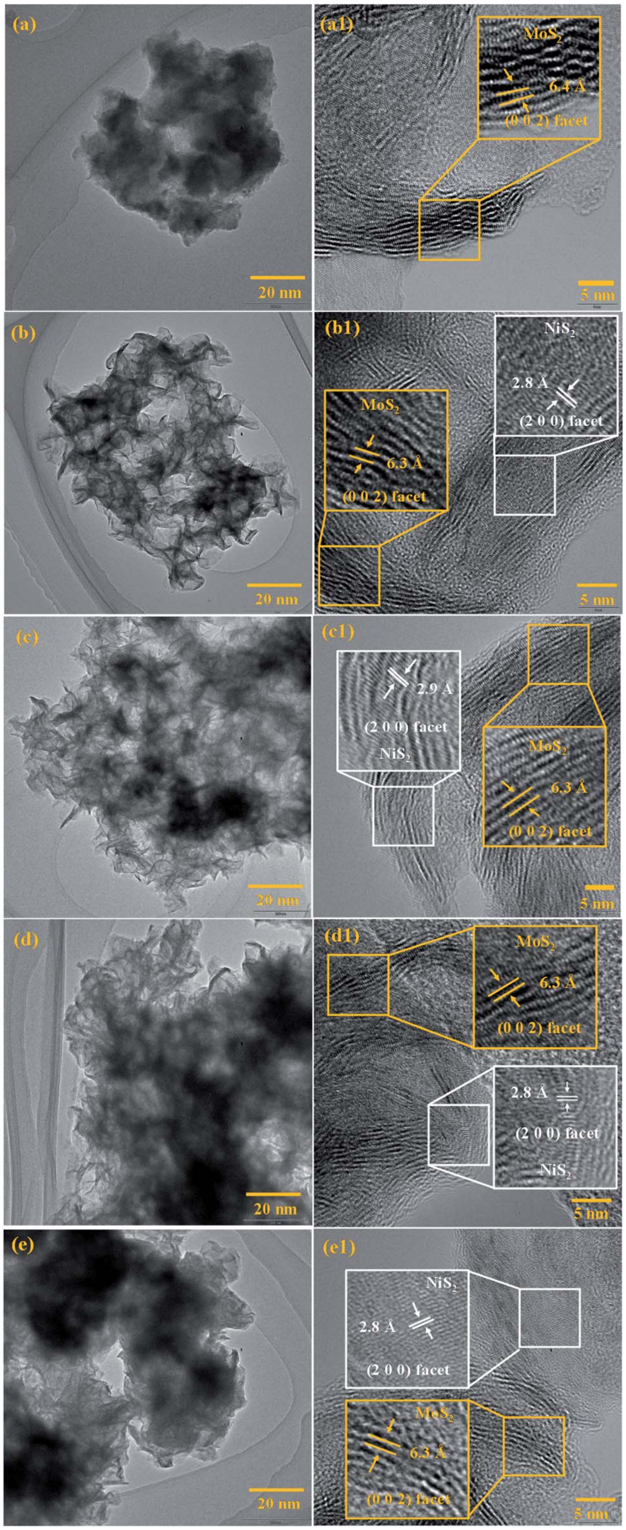

Fig. 5 (a–a1) HRTEM images of MoS_2, (b–e1) HRTEM images of MoS_2/NiS_2 nanocomposites with varied NiS_2 contents.

Based on the above results, growth mechanism has been proposed in Fig. 6. The formation of MoO_3 and S^{2-} ions obtained from the decomposition of sodium molybdate and thioacetamide. The reduction of Mo^{6+} to Mo^{4+} achieved at high

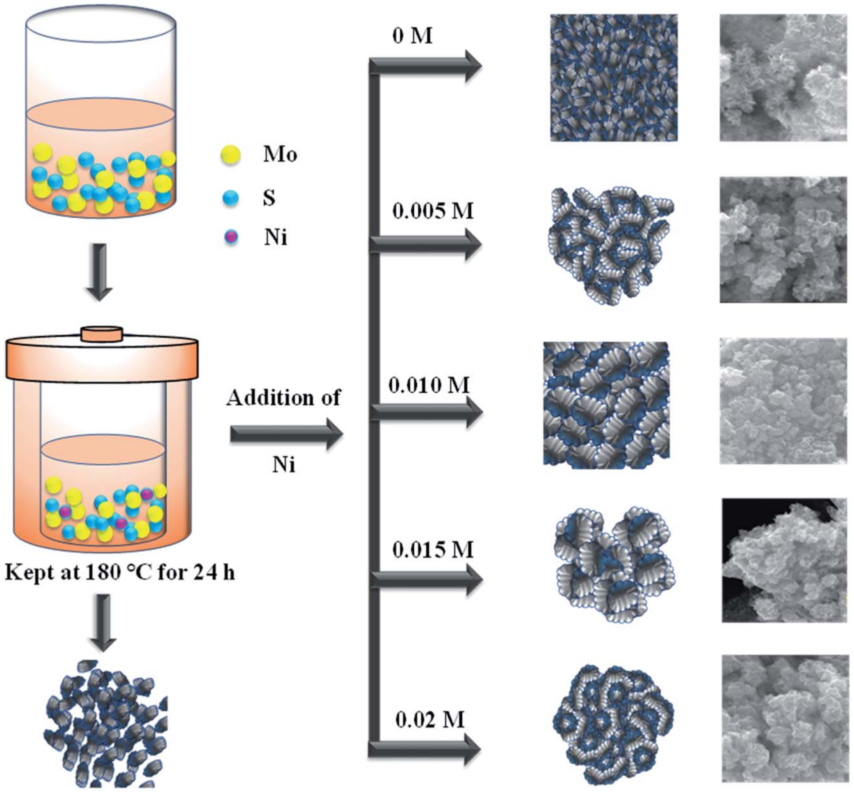

Fig. 6 Schematic representation of reaction mechanism.

temperature (180 °C). Mo^{4+} reacts with S^{2-} to form MoS_2 nanosheets.[33] In the case of MoS_2/NiS_2 composite, after the addition of Ni ions into the MoS_2 matrix, this leads to the growth towards (1 0 2) direction which was evident from the XRD results. Further increase in the Ni concentration, MoS_2 sheets shows more surface clearance and active edge sites which plays major role in photocatalytic activities.

3.5. Photocatalytic properties

Photocatalytic decomposition analysis was performed against RhB (target pollutant) dye using MoS_2 and MoS_2/NiS_2 catalysts under visible light irradiation. Before the photocatalytic degradation, adsorption–desorption equilibrium is achieved, and the concentration of RhB after adsorption is considered as the initial absorbance of RhB. The initial absorption peak centred at 554 nm gradually tends to decrease with the increase in irradiation time. The degradation profile has been plotted as time (t) *versus* C/C_0, where, C_0 is the initial concentration of RhB and C is the concentration of RhB concerning time t. Fig. 7(a) represents the maximum degradation percentage of the samples with respect to time. After 36 min of irradiation, the RhB was decomposed about 81.78%, 75.74% and 90.61% for MoS_2, Ni-2 and Ni-4 samples, respectively. It was evident that

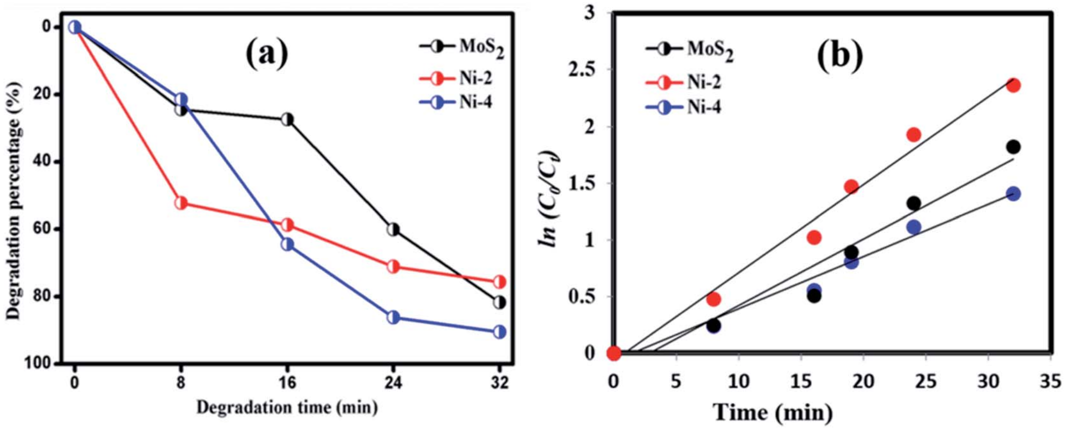

Fig. 7 (a) Plot of dye degradation (%) *versus* time and (b) plots of $\ln(C_0/C_t)$ as a function of time (min) of MoS_2/NiS_2 nanocomposites.

the degradation percentage considerably increased for Ni-4 sample.[34] For the comparison, photocatalytic performance was carried out for Ni-4 sample under direct solar light (Fig. S4†). The results obtained after 32 min confirms the degradation percentage of RhB was around 83.5% under direct solar light, which was less compared to the activity under xenon light source. The xenon light-driven photocatalyst shows the best activity due to more photon emission. To investigate whether the process obeyed pseudo-first-order kinetics, plots of $\ln(C_0/C_t)$ *versus* irradiation time for the adsorption and degradation of RhB on MoS_2/NiS_2 nanocomposites was examined. Fig. 7(b) shows the linear relationship for $\ln(C_0/C_t)$ plotted against irradiation time.

Based on the obtained results, the proposed photocatalytic mechanism for the RhB dye degradation by photocatalyst MoS_2/NiS_2 composites are shown below.

$$MoS_2/NiS_2 + h\nu \rightarrow NiS_2\ (h^+) + MoS_2\ (e^-) \tag{1}$$

$$O_2 + e^- \rightarrow {}^{\bullet}O_2^- \tag{2}$$

$$H_2O + h^+ \rightarrow {}^{\bullet}OH + H^+ \tag{3}$$

$${}^{\bullet}O_2^- + H_2O \rightarrow {}^{\bullet}HO_2 + OH^- \tag{4}$$

$${}^{\bullet}HO_2 + H_2O \rightarrow H_2O_2 + {}^{\bullet}OH \tag{5}$$

$$H_2O_2 \rightarrow 2{}^{\bullet}OH \tag{6}$$

$${}^{\bullet}OH + RhB \rightarrow CO_2 + H_2O + NO_3^- + NH_4^+ + Cl^- \tag{7}$$

The schematic (Fig. 8) illustrates the charge transfer mechanisms of MoS_2/NiS_2 under visible light irradiation. MoS_2 has a narrow bandgap (1.9 eV) semiconductor with a work function of 4.52 eV, whereas NiS_2 has a narrow bandgap semiconductor with a work function of 4.5 eV. Interface charge transfer mechanisms plays vital role in the degradation of organic pollutants. In MoS_2/NiS_2 nanocomposites, the number of interfaces has been increased with an increase in the concentration of NiS_2. Intercalation of NiS_2 in MoS_2 provides grate number of photogenerated electron–hole pairs.[35] Under visible light irradiation, electrons are excited from the valance band of NiS_2 to the conduction band, leaving behind holes in the valence band. The photoinduced electrons in the conduction band of NiS_2 were transferred to the conduction band of MoS_2, which acted as a photoelectronic receiver. The photogenerated holes reacted with either water (H_2O) or hydroxyl ions (OH) adsorbed onto the catalyst surface to produce hydroxyl radicals (${}^{\bullet}OH$), and the photogenerated electrons reacted with oxygen (O_2) to form superoxide radicals (${}^{\bullet}O_2$). Consequently, both OH, and ${}^{\bullet}O_2$ radicals can decompose the organic compounds which converts into CO_2, H_2O and other inorganic molecules as harmless compounds.[36]

To elucidate the photocatalytic activity under visible light, active species generated during the reaction were identified by free radical and hole scavenging experiments, which was shown in Fig. 9. Hydroxyl radical (${}^{\bullet}OH$), holes (h^+) and superoxide anions ($O_2^{-\bullet}$) are the possible active species in the photodegradation of organic pollutants. To detect the active species during the photocatalytic reaction, benzoic acid (BA), sodium salt of ethylenediamine tetraacetate (EDTA) and potassium persulfate ($K_2S_2O_8$) were introduced in the catalyst solution as

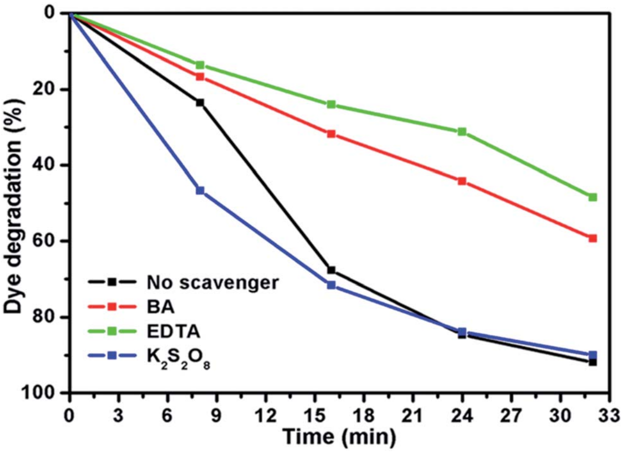

Fig. 9 Effect of RhB degradation over MoS_2/NiS_2 in the presence of various scavengers.

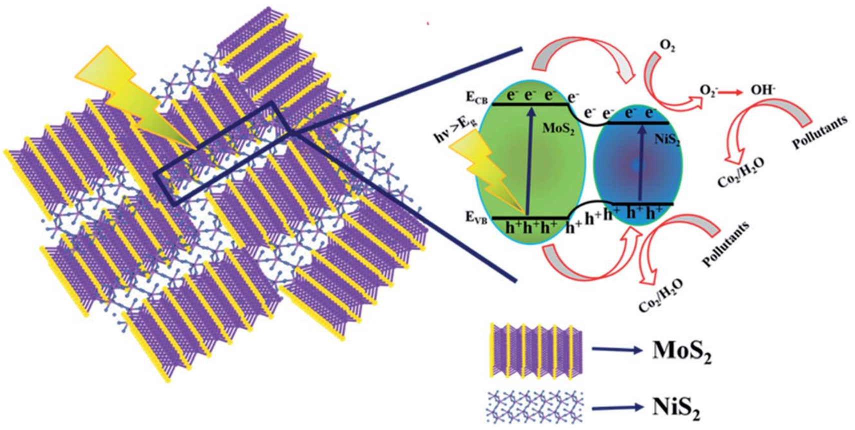

Fig. 8 Schematic charge transfer mechanism of MoS_2/NiS_2 nanocomposites.

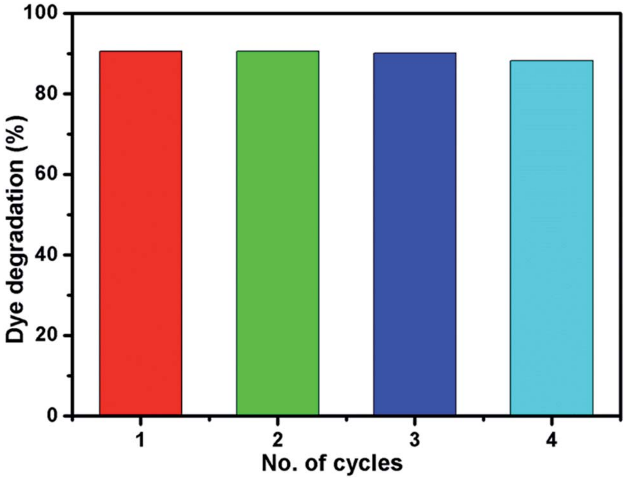

Fig. 10 Reusability of Ni-4 photocatalyst towards the degradation of RhB.

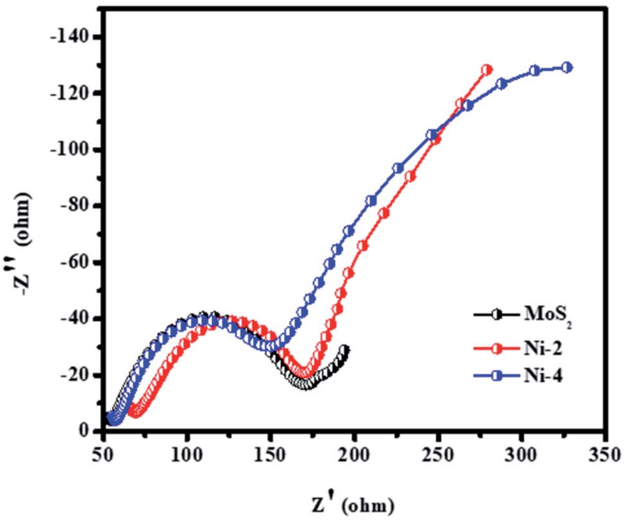

Fig. 11 Electrochemical impedance spectroscopy of MoS_2/NiS_2 nanocomposites with varied NiS_2 contents.

scavengers of hydroxyl radical, hole and superoxide radical anion, respectively.[37] Fig. 9 represents the photodegradation of RhB catalysed by MoS_2/NiS_2 (Ni-4) in the presence of these various scavengers under visible light illumination. Compared with the scavenger free system, the dye degradation efficiency in the presence of $^{\bullet}OH$ scavenger was 89%. In contrast, the reaction with the addition of EDTA scavenger was nearly inhibited with 48% of RhB degradation after 32 min. To further determine the degradation mechanism, another experiment was performed under BA scavenger. The photocatalytic activity was considerably reduced in the presence of the $O_2^{-\bullet}$ scavengers, where 59% RhB was degraded in 32 min. These results strongly suggest that hydroxyl radicals, holes and superoxide radical anions contributed to degrade the organic pollutant where hole (h^+) radical are the major oxidative species, responsible for the photooxidative conversion of RhB.[38,39]

Fig. 10 shows the reusability of Ni-4 photocatalyst towards the degradation of RhB examined over four cycles under visible light irradiation. After the photocatalysis experiment, the catalyst was separated from the reaction mixture by centrifugation and the concentration of the dye solution was adjusted to its initial value. Photocatalysts are reused for four cycles and the obtained degradation values are 90.61, 90.58, 90.5 and 89.92% for first, second, third and fourth cycles, respectively. It demonstrated that the synthesized sample can be used for multiple cycles in the photocatalysis process. In addition to that, we have investigated the structural property of the used catalyst (after the 4th cycle) by XRD analysis which was shown in Fig. S5.† The obtained XRD pattern exhibited the same peak positions as before the photocatalysis process which confirms the stability of the synthesized sample.

The interaction mechanism of an electron in the catalyst and electrolyte solution using electrochemical impedance spectroscopy (EIS) has been investigated. The measurement was studied using a three-electrode electrochemical cell (working electrode/reference electrode/counter electrode) with an alkaline electrolyte solution. Fig. 11 shows the Nyquist plot of the symmetric cells with different CEs and relevant equivalent circuit of respected cells. The charge transport resistance of the catalyst was calculated as 120 Ω for MoS_2, 100 Ω for Ni-2, and 95 Ω for Ni-4, respectively. The sample Ni-4 shows a low resistance value when compared with other samples, which clearly shows that sample Ni-4 has a more electrical and electrochemical property which was well-matched with dye degradation results.[40]

Table 1 Comparative photocatalytic performance of MoS_2/NiS_2 with other similar photocatalysts

Material	Morphology	Dye concentration (mg L^{-1})	Light source	Dye	Degradation (%)	Time taken (min)	Ref.
MoS_2	Porous microspheres	10	100 W xenon lamp	MB	89.2	150	38
MoS_2–TiO_2	Nanoparticles and nanocrystals	5	UV lamp	MB	61	100	14
ZnO/V_2O_5	Nanoparticles	10	—	MB	83	150	41
MoS_2/C_3N_4	Nano sheets	5	300 W xenon lamp	MO and RhB	—	—	42
Fe/Co doped TiO_2	Agglomerated particles	20	500 W Xe lamp	RhB	65	240	43
CdS	Quantum dots	20 ppm	125 W Hg lamp	RhB	82	60	44
MoS_2/NiFe	Nanosheets	20 ppm	UV lamp	RhB	90	120	45
g-C_3N_4	Nanosheets	200 ppm	125 W Hg visible lamp	RhB	90.2	60	46
$MoS_2/LaFeO_3$	Nanosheets	20	Direct sunlight	RhB	94	60	47
MoS_2/NiS_2	Nanosheets	20	400 W xenon lamp	RhB	90.6	32	This work

In 2-D layered materials, the size of the ultrathin nanosheets reason for the shortened transport distance, which results in an enhancement of charge transfer process. The driving force due to the internal electric field which results from the construction of semiconductor heterojunctions enables the separation and migration (transmission) of photogenerated carriers. The separation of electron–hole pairs can be efficiently promoted *via* the formation of 2D/2D architectures with a large contact area and a profound interface between them.[47,48] Previous investigations on similar materials employed for the degradation of organic pollutants are listed and compared in Table 1. Among them, MoS_2/NiS_2 composites studied in this work showed a maximum degradation efficiency of about 90.61% with a degradation time of 32 min.

4. Conclusion

The layered molybdenum disulfide (MoS_2) and molybdenum disulfide/nickel disulfide (MoS_2/NiS_2) nanocomposites were synthesized by hydrothermal method. The XRD patterns revealed the formation of hexagonal MoS_2 and cubic NiS_2. The morphological analysis confirmed the presence of layered MoS_2 nanostructures and interlaced MoS_2/NiS_2 nanostructures. The photocatalytic activity of MoS_2 and MoS_2/NiS_2 nanocomposites were studied against the degradation of RhB under visible-light irradiation. The maximum degradation efficiency of 90.61% was observed in 32 min for (Ni-4) MoS_2/NiS_2 nanocomposite sample.

Conflicts of interest

There are no conflicts to declare.

Acknowledgements

The authors thank the management of SRM IST for financial support. The authors thank Center for Instrumental Analysis, Shizuoka University, Hamamatsu, Japan for characterization facilities.

References

1 A. Iwase, H. Kato and A. Kudo, A Simple Preparation Method of Visible-Light-Driven $BiVO_4$ Photocatalysts From Oxide Starting Materials Bi_2O_3 and V_2O_5 and Their Photocatalytic Activities, *J. Sol. Energy Eng.*, 2010, **132**, 021106.

2 M. Sabarinathan, S. Harish, J. Archana, M. Navaneethanb, H. Ikeda and Y. Hayakawa, Controlled exfoliation of monodispersed MoS_2 layered nanostructures by ligand-assisted hydrothermal approach for the realization of ultrafast degradation of organic pollutant, *RSC Adv.*, 2016, **6**, 109495–109505.

3 C. Guillard, H. Lachhe, A. Hou, M. Ksibi, E. Elaloui and J. M. Herrmann, Influence of chemical structure of dyes, of pH and of inorganic salts on their photocatalytic degradation by TiO_2 comparison of the efficiency of powder and supported TiO_2, *J. Photochem. Photobiol., A*, 2003, **158**, 27–36.

4 S. Kaur, S. Sharma, A. Umar, S. Singh, S. K. Mehta and S. K. Kansal, Solar light driven enhanced photocatalytic degradation of brilliant green dye based onZnS quantum dots, *Superlattices Microstruct.*, 2017, **103**, 365–375.

5 D. A. Shende, Y. N. Rane, M. G. Raghuwanshi, N. M. Gosavi, S. R. Gosavi and N. G. Deshpande, Visible-light-driven photocatalytic activity of mixed phase CdS-flakes, *Optik*, 2018, **161**, 284–292.

6 C. Ramamoorthy and V. Rajendran, Synthesis and characterization of CuS nanostructures: structural, optical, electrochemical and photocatalytic activity by the hydro/solvothermal process, *Int. J. Hydrogen Energy*, 2017, **42**, 26454–26463.

7 H. Hwang, H. Kim and J. Cho, MoS_2Nanoplates Consisting of Disordered Graphene-like Layers for High Rate Lithium Battery Anode Materials, *Nano Lett.*, 2011, **11**, 4826–4830.

8 J. Xiao, D. Choi, L. Cosimbescu, P. Koech, J. Liu and J. P. Lemmon, Exfoliated MoS_2 Nanocomposite as an Anode Material for Lithium Ion Batteries, *Chem. Mater.*, 2010, **22**, 4522–4524.

9 C. Wang, B. Tian, M. Wu and J. Wang, Revelation of its Excellent Intrinsic Activity of $MoS_2|NiS|MoO_3$,Nanowire for Hydrogen Evolution Reaction in Alkaline, *ACS Appl. Mater. Interfaces*, 2017, **9**, 7084–7090.

10 Y. H. Hung, A. Y. Lu, Y. H. Chang, J. K. Huang, J. K. Chang, L. J. Li and C.-Y. Su, Scalable Patterning of MoS_2Nanoribbons by Micromolding in Capillaries, *ACS Appl. Mater. Interfaces*, 2016, **8**, 20993–21001.

11 Z. He and W. Que, Molybdenum disulfide nanomaterials: structures, properties, synthesis and recent progress on hydrogen evolution reaction, *Appl. Mater. Today*, 2016, **3**, 23–56.

12 U. T. D. Thuy, N. Q. Liem, C. M. A. Parlett, G. M. Lalev and K. Wilson, Synthesis of CuS and CuS/ZnS core/shell nanocrystals for photocatalytic degradation of dyes under visible light, *Catal. Commun.*, 2014, **44**, 62–67.

13 Y. H. Tan, K. Yu, J. Z. Li, H. Fu and Z. Q. Zhu, MoS_2@ZnO nano-heterojunctions with enhanced photocatalysis and field emission properties, *J. Appl. Phys.*, 2014, **116**, 064305.

14 I. Tacchini, E. Terrado, A. Ansón and M. T. Martínez, Preparation of a TiO_2–MoS_2 nanoparticle-based composite by solvothermal method with enhanced photoactivity for the degradation of organic molecules in water under UV light, *Micro Nano Lett.*, 2011, **6**, 932–936.

15 Y. Ding, Y. Zhou, W. Nie and P. Chen, MoS_2–GO nanocomposites synthesized via a hydrothermal hydrogel method for solar light photocatalytic degradation of methylene blue, *Appl. Surf. Sci.*, 2015, **357**, 1606–1612.

16 H. Feng, W. Zhou, X. Zhang, S. Zhang, Bo Liu and D. Zhen, Synthesis of Z-scheme Mn–CdS/MoS2/TiO2 ternary photocatalysts for high-efficiency sunlight-driven photocatalysis, *Adv. Compos. Mater.*, 2019, **28**, 2633366X19895020.

17 W. Y. Lim, M. Hong and G. W. Ho, In situ photo-assisted deposition and photocatalysis of $ZnIn_2S_4$/transition metal

chalcogenides for enhanced degradation and hydrogen evolution under visible light, *Dalton Trans.*, 2016, **45**(2), 552–560.

18 X. Li, S. Zhang, X.-J. Wang, G.-F. Huang, Li-X. Xia, W. Hu and W.-Q. Huang, A two-dimensional MoS_2/SnS heterostructure for promising photocatalytic performance: first-principles investigations, *Phys. E*, 2020, 114453.

19 X. Chen, J. Zhang, J. Zeng, Y. Shi, S. Lin, G. Huang, H. Wang, Z. Kong, J. Xi and Z. Ji, MnS coupled with ultrathin MoS_2 nanolayers as heterojunction photocatalyst for high photocatalytic and photoelectrochemical activities, *J. Alloys Compd.*, 2019, **771**, 364–372.

20 X.-L. Yin, S.-R. Han and L.-L. Li, CdS@MoS_2 core@shell nanorod heterostructures for efficient photocatalytic pollution degradation with good stability, *Optik*, 2020, **220**, 165252.

21 Y. Yang, K. Zhang, H. Lin, X. Li, H. C. Chan, L. Yang and Q. Gao, MoS_2–Ni_3S_2 Hetero nanorods as Efficient and Stable Bi-functional Electrocatalysts for Overall Water Splitting, *ACS Catal.*, 2017, **7**, 2357–2366.

22 A. Molla, M. Sahu and S. Hussain, Synthesis of Tunable Band Gap Semiconductor Nickel Sulphide Nanoparticles: Rapid and Round the Clock degradation of Organic Dyes, *Sci. Rep.*, 2016, **6**, 26034.

23 T. Storr and R. Mukherjee, Preface for the forum on applications of metal complexes with ligand-centered radicals, *Inorg. Chem.*, 2018, 9577–9579.

24 B. Baral and K. Parida, {040/110} Facet Isotype Heterojunctions with Monoclinic Scheelite $BiVO_4$, *Inorg. Chem.*, 2020, **59**(14), 10328–10342.

25 C. Wei, C. Cheng, Y. Cheng, Y. Wang, Y. Xu, W. Du and H. Pang, Comparison of NiS_2 and supercapacitors, non-enzymatic glucose sensors and water treatment, *The Royal Society of Chemistry*, 2013, **44**, 17278–17285.

26 G. Swain, S. Sultana, B. Naik and K. Parida, Coupling of crumpled-type novel MoS_2 with CeO_2 nanoparticles: a noble-metal-free p–n heterojunction composite for visible light photocatalytic H2 production, *ACS Omega*, 2017, **2**(7), 3745–3753.

27 S. Mansingh, D. K. Padhi and K. M. Parida, Enhanced photocatalytic activity of nanostructured Fe doped CeO_2 for hydrogen production under visible light irradiation, *Int. J. Hydrogen Energy*, 2016, **41**(32), 14133–14146.

28 B. Li, L. Jiang, X. Li, P. Ran, P. Zuo, A. Wang, L. Qu, Y. Zhao, Z. Cheng and Y. Lu, Preparation of Monolayer MoS_2 Quantum Dots using Temporally Shaped Femtosecond Laser Ablation of Bulk MoS_2 Targets in Water, *Sci. Rep.*, 2017, **7**, 11182.

29 J. Lin, P. Wang, H. Wang, Li Chun, X. Si, J. Qi, J. Cao, Z. Zhong, W. Fei and J. Feng, Defect-Rich Heterogeneous MoS_2/NiS_2 Nanosheets Electrocatalysts for Efficient Overall Water Splitting, *Adv. Sci.*, 2019, **6**, 1900246.

30 H. Peng, D. Liu, X. Zheng and X. Fu, N-doped carbon-coated ZnS with sulfur-vacancy defect for enhanced photocatalytic activity in the visible light region, *Nanomaterials*, 2019, **9**, 1657.

31 N. Jiang, Q. Tang, M. Sheng, B. You, D. Jiang and Y. Sun, Nickel sulfides for electrocatalytic hydrogen evolution under alkaline conditions: a case study of crystalline NiS, NiS_2, and Ni_3S_2 nanoparticles, *Catal. Sci. Technol.*, 2016, **6**, 1077–1084.

32 S. Subudhi, G. Swain, S. P. Tripathy and K. Parida, UiO-66-NH_2 Metal–Organic Frameworks with Embedded MoS_2 Nanoflakes for Visible-Light-Mediated H_2 and O_2 Evolution, *Inorg. Chem.*, 2020, **59**(14), 9824–9837.

33 Qu Zhou, C. Hong, Y. Yao, S. Hussain, L. Xu, Q. Zhang, Y. Gui and M. Wang, Hierarchically MoS_2 nanospheres assembled from nanosheets for superior CO gas-sensing properties, *Mater. Res. Bull.*, 2018, **101**, 132–139.

34 P. Liu, Y. Liu, W. Ye, J. Ma and D. Gao, Flower-like N-doped MoS_2 for photocatalytic degradation of RhB by visible light irradiation, *Nanotechnology*, 2016, **27**, 225403.

35 H. Feng, W. Zhou, X. Zhang, S. Zhang, Bo Liu and D. Zhen, Synthesis of Z-scheme Mn–CdS/MoS_2/TiO_2 ternary photocatalysts for high-efficiency sunlight-driven photocatalysis, *Adv. Compos. Mater.*, 2019, **28**, 2633366X19895020.

36 A. M. Huerta-Flores, M. T.-M. Leticia, E. Moctezuma, A. P. Singh and B. Wickman, Green synthesis of earth-abundant metal sulfides (FeS_2, CuS, and NiS_2) and their use as visible-light active photocatalysts for H_2 generation and dye removal, *J. Mater. Sci.: Mater. Electron.*, 2018, **29**(13), 11613–11626.

37 G. Gong, Y. Liu, B. Mao, B. Wang, L. Tan, D. Li, Y. Liu and W. Shi, Mechanism study on the photocatalytic efficiency enhancement of MoS_2 modified Zn–$AgIn_5S_8$ quantum dots, *RSC Adv.*, 2016, **6**(101), 99023–99033.

38 Y. Lin, Z. Zhou, P. Zhang, E. Ashalley, M. Shafa, H. Li, J. Wu and Z. Wang, Hydrothermal fabrication of porous MoS_2 and its visible light photocatalytic properties, *Mater. Lett.*, 2014, **131**, 122–124.

39 J. Li, X. Liu, L. Pan, W. Qin, T. Chena and Z. Sun, MoS_2–reduced graphene oxide composites synthesized via a microwave-assisted method for visible-light photocatalytic degradation of methylene blue, *RSC Adv.*, 2014, **4**, 9647–9651.

40 J. Wang, L. Zheng, C. Zhan, K. Zhang, X. Lai, J. Tu and Y. Cao, 3D hierarchical NiS_2/MoS_2 nanostructures on CFP with enhanced electrocatalytic activity for hydrogen evolution reaction, *J. Mater. Sci. Technol.*, 2020, **39**, 155–160.

41 C. W. Zou, Y. F. Rao, A. Alyamani, W. Chu, M. J. Chen, D. A. Patterson, E. A. C. Emanuelsson and W. Gao, Heterogeneous Lollipop-like V_2O_5/ZnO Array: A Promising Composite Nanostructure for Visible Light Photocatalysis, *Langmuir*, 2010, **26**, 11615–11620.

42 Q. Li, N. Zhang, Y. Yang, G. Wang and D. H. L. Ng, High Efficiency Photocatalysis for Pollutant Degradation with MoS_2/C_3N_4 Heterostructures, *Langmuir*, 2014, **30**, 8965–8972.

43 Z. Wang, C. Chen, F. Wu, B. Zou, M. Zhao, J. Wang and C. Feng, Photodegradation of rhodamine B under visible light by bimetal codoped TiO_2 nanocrystals, *J. Hazard. Mater.*, 2009, **164**, 615–620.

44 D. Kandi, S. Martha, A. Thirumurugan and K. M. Parida, Modification of BiOI microplates with CdS QDs for enhancing stability, optical property, electronic behavior toward rhodamine B decolorization, and photocatalytic hydrogen evolution, *J. Phys. Chem. C*, 2017, **121**(9), 4834–4849.

45 S. Nayak, G. Swain and K. Parida, Enhanced photocatalytic activities of RhB degradation and H_2 evolution from in situ formation of the electrostatic heterostructure MoS_2/NiFe LDH nanocomposite through the Z-Scheme mechanism via p–n heterojunctions, *ACS Appl. Mater. Interfaces*, 2019, **11**(23), 20923–20942.

46 S. Martha, S. Mansingh, K. M. Parida and A. Thirumurugan, Exfoliated metal free homojunction photocatalyst prepared by a biomediated route for enhanced hydrogen evolution and rhodamine B degradation, *Mater. Chem. Front.*, 2017, **1**(8), 1641–1653.

47 S. Acharya, G. Swain and K. M. Parida, MoS_2-mesoporous $LaFeO_3$ hybrid photocatalyst: highly efficient visible-light driven photocatalyst, *Int. J. Hydrogen Energy*, 2020, 11502–11511.

48 H. Hao and X. Lang, Metal Sulfide Photocatalysis: Visible-Light-Induced Organic Transformations, *ChemCatChem*, 2019, **11**(5), 1378–1393.